



PCCP

Structural search for stable Mg-Ca alloys accelerated with a neural network interatomic model

Journal:	<i>Physical Chemistry Chemical Physics</i>
Manuscript ID	CP-ART-08-2018-005314.R1
Article Type:	Paper
Date Submitted by the Author:	05-Oct-2018
Complete List of Authors:	Ibarra Hernández, Wilfredo; Benemerita Universidad Autonoma de Puebla, Facultad de Ingenieria; West Virginia University, Department of Physics and Astronomy Hajinazar, Samad; Binghamton University, Department of Physics, Applied Physics and Astronomy Avendaño-Franco, Guillermo; West Virginia University, Department of Physics and Astronomy Bautista-Hernandez, Alejandro; Benemerita Universidad Autonoma de Puebla, Facultad de Ingeniería Kolmogorov, Alexey ; Binghamton University, Romero, Aldo; West Virginia University, Physics; Benemerita Universidad Autonoma de Puebla,





Cite this: DOI: 10.1039/xxxxxxxxxx

Structural search for stable Mg-Ca alloys accelerated with a neural network interatomic model[†]

Wilfredo Ibarra-Hernández,^{*ab} Samad Hajinazar,^c Guillermo Avendaño-Franco,^b Alejandro Bautista-Hernández,^a Aleksey N. Kolmogorov,^{*c} and Aldo H. Romero^{*ab}

Received Date

Accepted Date

DOI: 10.1039/xxxxxxxxxx

www.rsc.org/journalname

We have combined a neural network formalism with metaheuristic structural global search algorithms to systematically screen the Mg-Ca binary system for new (meta)stable alloys. The combination of these methods allows for an efficient exploration of the potential energy surface beyond the possibility of the traditional searches based on *ab initio* energy evaluations. The identified pool of low-enthalpy structures was complemented with special quasirandom structures (SQS) at different stoichiometries. In addition to the only Mg-Ca phase known to form under standard synthesis conditions, C14-Mg₂Ca, the search has uncovered several candidate materials that could be synthesized under elevated temperatures or pressures. We show that the vibrational entropy lowers the relative free energy of several phases with magnesium kagome layers: C15 and C36 Laves structures at the 2:1 composition and an orthorhombic oS36 structure at the 7:2 composition. The estimated phase transition temperatures close to the melting point leaves open the possibility of synthesizing the predicted materials at high temperatures. At high pressures up to 10 GPa, two new phases at the 1:1 and 3:1 Mg:Ca stoichiometries become thermodynamically stable and should form in multi-anvil experiments.

1 Introduction

High strength and low density together with good stiffness are some of the preferred properties that motivate the scientific research of new structural materials for the automotive and aircraft industry.¹ Among the possible candidates, Mg alloys are considered as very promising compounds since Mg is one of the lightest structural materials with a density of 1.74g/cm³ making it attractive in different applications where weight is a critical requirement.² This element has a number of other desirable features, such as easy recyclability, high natural abundance (eight most abundant element in the Earth's crust), good heat transfer, and high specific strength.^{3,4} However, this element also shows many drawbacks that limit its usability in current technologies. Low ignition resistance, corrosion, discrete properties at high temperatures, low ductility, among others are the main challenges that have to be overcome to increase the usability of Mg.⁵ One

of the widely used methods to improve the mechanical properties of Mg is through alloying.^{6–8} We have recently proposed a strategy for selecting suitable alloying agents. We argued that the low ductility of Mg is inherent of its hexagonal crystal structure and that the choice of alloying metals with cubic elemental ground states could stabilize Mg compounds in cubic structures.⁹ In our previous publication, we used the minima hopping method (MHM) combined with *ab-initio* calculations to search for crystal structures at different lithium alloying concentrations, considering only up to 16 atoms per unit cell.⁹ We found that there were only a few low energy structures with cubic-like symmetry, which indicates that lithium alloying was not enough to drive the basic crystal structure to a cubic-like structure or that disorder is also playing a major role in the synthesis of this alloy, a possibility that was not explored in ref.⁹

Recent efforts focused on improving the mechanical strength, ductility, and corrosion resistance of Mg alloys include the study of solid solutions of Mg with rare earth and transition metals. However, these alloying elements are expensive and difficult to handle which could make them unsuitable for technological applications.^{10,11} On the other hand, the most used magnesium alloy is the so-called AZ91 (Mg-9wt%Al-1wt%Zn). Mg-Al alloys possess modest tensile properties and their usability is limited to low temperatures due to their poor heat resistance.⁵ Mg-Al doped with Ca has exhibited improved heat resistance¹² while Mg al-

^a Facultad de Ingeniería-BUAP, Apartado Postal J-39, Puebla, Pue. 72570, México

^b Department of Physics and Astronomy, West Virginia University, Morgantown, WV-26505-6315, USA

^c Department of Physics, Applied Physics and Astronomy, Binghamton University, State University of New York, PO Box 6000, Binghamton, New York 13902-6000, USA

[†] Electronic Supplementary Information (ESI) available. See DOI: 10.1039/b000000x/

* E-mail: wilfredo.ibarra@correo.buap.mx, kolmogorov@binghamton.edu, alromero@mail.wvu.edu

loyed directly with Ca has shown good oxidation and combustion resistance.^{13,14}

Theoretical and experimental results indicate that the only stable Mg-Ca alloy under ambient conditions is a C14-Mg₂Ca Laves phase.¹⁵ C14-Mg₂Ca has space group #194 with 4 chemical formula units per unit cell. Mg atoms are located at the *2a* and *6h* Wyckoff positions while Ca atoms are at the *4f* sites, with experimental lattice parameters of 6.22Å and 10.10Å.¹⁶ Recent entropy and heat capacity theoretical calculations show an excellent agreement with experimental measurements for the C14 structure.¹⁷ Pressure effects have been considered for this stoichiometry and the ductile character of Mg₂Ca has been confirmed.¹⁸ Other select Mg-Ca compositions have also been considered in recent computational studies^{17–21} but, to the best of our knowledge, no systematic structural screening based on unconstrained structure searches has yet been performed for the full Mg-Ca concentration range at high pressures.

Laves phases C14, C15, and C36 for the Mg₂Ca alloy have been extensively studied in previous theoretical works.^{15,22} Laves phases are structurally related to each other, and the main difference between them is the stacking sequence.²³ While C15 is cubic with space group #227 (*Fd $\bar{3}m$* with stacking sequence ABC), C14 and C36 are hexagonal with space group #194 (*P6₃/mmc* with stacking sequences AB and ABAC, respectively). The close relation between these structures is more evident when the cubic C14 phase is represented as a rhombohedral structure in its hexagonal representation. Since the three Laves phases are closely related structurally, it is not surprising that they have similar energy.^{22,24–26} The formation energy difference between C14 and C15 (with C36 midway between them) is only 3–4 meV/atom^{17,21,22} but neither the C36 nor the C15 Laves phase has been experimentally found in Mg₂Ca. It is important to investigate whether there are achievable pressure and temperature conditions under which the synthesis of the alternative structure types is possible for this binary compound.

Structural phase transitions among Laves phases have been reported in numerous systems.²⁷ This behavior has been observed in binary compounds such as Cr-Hf^{28,29}, Cr-Zr^{30,31}, Hf-Mo^{32,33}, Co-Nb³⁴, among others. Many of these systems show a C15 to C14 transformation with increasing temperature, while the C36 structure was considered as an intermediate phase. The only exception found in the literature to this behavior is in ThMg₂, where the transition was from C36 to C15.³⁵ It has been reported that ScFe₂ goes through a phase transition from the low temperature structure C14 to the cubic C15 and ultimately to the hexagonal C36.³⁶ Other experimental works show that the transition is from C14 to C36, which implies that the cubic C15 structure can only be achieved at off-stoichiometric composition of 36.5.at.% Sc in a temperature range of 1295 and 1525 C.³⁷ The phase transformations are not exclusively temperature-dependent, as they have also been observed under pressure.^{38–40} It has been reported that ZrFe₂ transforms from the hexagonal C36 to the cubic C15 as a consequence of Shockley partial dislocations.^{41,42} Even though theoretical calculations have successfully reproduced the ground state Laves phase for some of the mentioned compounds^{22,43}, such calculations have been restricted to stoichiometric composi-

tions at zero temperature.

The purpose of this work is a systematic identification and characterization of new (meta)stable alloys across a wide Mg-Ca composition range. The structures have been obtained through the sampling of the potential energy surface (PES) using two different search methodologies, the MHM and Firefly (FF) method. We have also compared the reliability and accuracy of the neural network (NN) formalism implemented in MAISE with respect to *ab initio* results. Our developed NN model has been used to predict the convex hull of Mg-Ca alloys at different pressure values. We have identified several metastable phases and for some of them we discussed the structural morphology, electronic band structure, and phonon dispersion features. Due to the computational requirements of *ab initio* calculations, structural searches with unit cells larger than about 16 atoms become computationally demanding. The use of the NN interatomic potential has allowed us to expand the configurational search space greatly by considering unit cells with up to 28 atoms. The limit was set to reduce the number of possible concentrations for the binary system. The linear scaling of the NN model's cost with the system size has also been beneficial in our calculations involving particularly large unit cells. We calculated vibrational properties for a number of large supercells with up to 576 atoms and assessed the role of disorder by considering more than 100 special quasirandom structures (SQS)⁴⁴ with up to 216 atoms.

We show that besides the well known and well studied Laves phase C14-Mg₂Ca, there are other possible Mg-Ca compositions with different crystal symmetries which are at least metastable and that could appear under certain synthesis conditions. To take advantage of the search results at low pressures, we have used all the structures found at 5 GPa (around 70,000 structures) as input to perform local geometry optimization at 0 and 10 GPa and to obtain the corresponding convex hulls.

In Section II, we detail the computational methods benchmarked and used in this work. In Section III, we describe the results of our structure searches and discuss the stability of select phases in the 0-10 GPa pressure range. In Section IV, we present our analysis of structural, vibrational, and electronic properties for several (meta)stable Mg-Ca phases.

2 Methods

2.1 Theoretical details of *ab-initio* calculations

Before giving a detailed description of the methods used in the structural search, we summarize the settings used in the density functional theory (DFT)^{45,46} calculations. For such, we have used the Vienna *ab-initio* Simulation Package (VASP),^{47–49} to perform structural relaxation and energy evaluation. The same methodology has been employed to generate datasets for the NN parameterization. We have chosen the number of k-points⁵⁰ in dependency of the size of the crystal structure to discretize the reciprocal space. We have used a high plane-wave energy cutoff of 500 eV to ensure convergence in energy and forces. With respect to the pseudopotentials, we used the projector-augmented wave (PAW)^{51,52} method and the generalized gradient approximation (GGA) to the exchange-correlation energy with the Perdew-

Burke-Ernzerhof (PBE) parametrization. The Mg_{pv} and Ca_{pv} PAW pseudopotentials have Xp^6Ys^2 orbitals as part of the valence shell, where X and Y equals to 2 and 3 (3 and 4) for magnesium (calcium). The method of cell relaxation under zero or hydrostatic pressure was the BFGS⁵³ for VASP and MAISE.⁵⁴

Phonon calculations have been performed with Phonopy⁵⁵ and PHON⁵⁶ packages. We relied on the quasiharmonic approximation in the frozen phonon approach. Accurate evaluation of interatomic force constants typically requires force calculations in supercells of at least 100 atoms. A $10^3 - 10^4$ -fold speed-up achieved with the NN formalism over the DFT for supercells of such size has allowed us to examine vibrational properties in several Mg-Ca phases. As can be seen in our previous⁵⁷ and present (Fig. S3) comparison tests, the developed NN models provide a reliable description of vibrational properties. For selected (near)-stable phases, we calculated vibrational contributions to the free energy with both formalisms, while the phonon dispersion for (meta)-stable structures were calculated with the NN formalism unless specified otherwise.

2.2 Minima Hopping and Firefly method

The crystal structure prediction based only on the chemical composition relies on two different and independent elements: (i) the level of theory used to describe the potential energy surface (PES), providing the crystal total energy, interatomic forces, and stresses in the considered unit cell and (ii) the algorithm used to explore the high dimensional PES. This search has to be performed as efficiently as possible, and we achieve this by exploring regions with energy wells instead of energy cusps and with a large structure diversity, which enables the consideration of a variety of atomic motifs.

The MHM⁵⁸ is one of the many proposed global structural search methods that has been developed in recent years. We have used a combination of MHM and DFT calculations to sample the PES for testing the reliability of the FF predictions when coupled to the NN framework. MHM is an efficient algorithm that makes use of short molecular dynamic (MD) simulations to explore the PES. The MD simulation helps to escape from local minima by aligning the MD initial velocities along the soft modes. These velocities will kick the dynamics and evolve the structure by changing atomic positions and cell parameters. After each escape move, a full structural relaxation is performed. To avoid revisiting the same minima, this method uses a Taboo mechanism, which keeps a list of visited minima such that only new minima are accepted at each step during the search. This methodology has proven its reliability in different binary compounds with up to 20 atoms per cell as in Li-Mg⁹ and also in compounds with strong spin-orbit interaction as Bi-Sb⁵⁹ where a Weyl semimetallic state has been predicted.⁶⁰

For the full-scale exploration of the binary Mg-Ca system, we have used the FF as implemented in the PyChemia package.^{61,62} The FF method is a stochastic global search algorithm that mimics the mating strategy of fireflies. It directs a population of candidates (chosen randomly from a predefined database of potential crystal phases or randomly generated) towards low-energy basins

by changing lattice parameters and atomic positions of structures relaxed to their respective local minima. The amount of movement towards low energy (enthalpy) candidates is proportional to the distance between two candidates. This distance is also used as a measure to determine if the two configurations are equivalent. At each iteration, high energy structures are replaced by new ones. The whole purpose of the algorithm is to promote the exploration of promising regions of the PES and still offer the possibility of exploring diverse morphologies with the continuous generation of new random structures. Details on the Pychemia-MAISE interface as well as an extended explanation of the creation of structures for each generation can be found in the Supplemental Information.⁶³ Details on the FF implementation and parameters used in this work and how the analysis is performed can be found in ref.⁶¹.

2.3 Parameterization of the Mg-Ca neural network interatomic model

Ab initio dataset Neural networks have recently attracted a considerable renewed interest in materials modeling.^{57,64-73} While the accuracy of traditional classical potentials is determined mainly by the physics embedded into their rigid functional forms, the performance of NN-based interatomic models is defined largely by the accuracy, diversity, and extent of the reference data sets. With the primary goal of using NN models for unconstrained structure optimization, we have recently introduced and tested an approach for automated generation of relevant data sets based on mock evolutionary searches.⁵⁷ In this procedure, small-size structures with unit cells containing 1-6 atoms for unaries and 2-11 atoms for binaries are generated randomly and evolved with mutation operations over 10-25 generations. In order to avoid oversampling of near-equilibrium configurations, we allow only a few relaxation steps in local unit cell optimizations. Structural diversity is additionally promoted by elimination of similar entries based on the radial distribution function.^{74,75} As detailed in our previous study⁵⁷, inclusion of small 'equation of state' sets for select low-enthalpy structures helps ensure a robust description of short-distance configurations encountered in unconstrained searches. The total Mg-Ca training set with target DFT enthalpies comprises over 40,000 structures generated primarily with the evolutionary sampling for hydrostatic pressures in the 0-50 GPa range (see Table 1 and Fig. 1).

We would like to note that it is possible to construct NN models with higher accuracy⁶⁹ by favoring particular structural motifs in the generation of reference data sets. Our early tests indicated that NN models fitted to such data tend to have numerous artificial minima in the regions of the PES frequently visited during unconstrained searches. Finding a reasonable trade-off between accuracy and reliability was a key consideration in the tuning of our automated data generation scheme that samples configurations from multiple relevant basins. Similar approaches have been explored in recent studies by other groups.^{71,76}

Descriptor and NN specifications A distinct feature of NN-based interatomic models is the requirement for input vectors describing relevant atomic environments to have constant length.⁵⁷ The

mapping of nearest neighbor distributions must also be invariant under translation, rotation, and identical atom swap. A *descriptor* proposed by Behler and Parrinello is a set of symmetry functions summed over atom pairs and triplets within a cut-off radius.⁶⁴ We have chosen a set of 51 Behler-Parrinello symmetry functions⁶⁴ that were tested and described in our previous study.⁵⁷ Due to the relatively large size of Mg and Ca, we extended the standard 6.0 Å cut-off radius to 7.5 Å and reduced all η parameters by a factor of 1.25² accordingly. The NN was a standard 2-layer perceptron with 15 neurons per layer. However, the NN parameterization was done using our recently proposed stratified training⁵⁷: unary Mg and Ca parameters were fitted first using the corresponding unary data and then kept fixed during fitting of the Mg-Ca parameters. The procedure enables re-use of the NN models in other multi-component systems in the future. Table 1 summarizes the number of adjustable parameters and reference data points used at each stage.

NN test results We have carried out a standard set of calculations⁵⁷ to test the performance of the developed NN. Fig. 2 shows distributions of errors for structures not included in the training set. As expected, the largest deviations are observed for high-energy structures but the NN performance remains reasonably accurate across the sampled 2-3 eV/atom range. Equation of state data for select structures in Fig. S1 illustrates further that the NN model correctly describes atomic environments uncommon for the Mg and Ca metals, such as the low-coordination configurations in the β -Sn and diamond structures. The B1-MgCa phase, not explicitly included in the training set and found to be 322 meV/atom above B2-MgCa in the DFT treatment, is described considerably better with the NN model (within 13 meV/atom) than with the MEAM potential¹⁹ (more than 90 meV/atom). The vacancy and substitution formation energies plotted in Fig. S2 are reproduced within 0.1-0.2 eV/defect; as discussed in our previous work⁵⁷, such accuracy is consistent with the 5-10 meV/atom overall accuracy of the NN models. The NN model is also in a

good agreement with the DFT describing equilibrium structural parameters. The fully optimized C14-Mg₂Ca lattice constants a and c are 6.243 Å and 10.076 Å at the NN level and $a = 6.238$ Å and 10.072 Å in our DFT calculations. For comparison, the experimental values are 6.22 Å and 10.10 Å, respectively.¹⁶

Table 1 Standard deviation in DFT data sets, number of structures used for NN training, number of adjustable NN parameters, and training/testing errors for the corresponding NNs.

Data set	ΔE^{data} eV/atom	No. of data	No. of weights	ΔE^{train} meV/atom	ΔE^{test} meV/atom
Mg	0.438	13878	1036	2.82	2.84
Ca	0.720	13688	1036	5.43	6.24
MgCa	0.788	14033	2820	6.46	7.19

2.4 Special Quasirandom structures (SQS)

Most structural search methods are quite efficient in exploring stable and metastable configurations of crystal phases of a given chemical compound. Some algorithms start with fully random unit cells while others from ordered phases. Independently of the starting point, the chosen method will try to search for an ordered crystal, as the considered unit cells are small and the periodic boundary conditions impose symmetry constraints in the structural minimization. In order to examine the energetic competition between low symmetry and substitutional disorder in random alloys, a different approach needs to be considered. In this work, we complemented our structural searches with simulations of substitutional disorder as a possible stabilization factor for Mg-Ca compounds. As the complexity of a random alloy with substitutional disorder grows exponentially with the number of sites, we have used the methodology introduced by Zunger⁴⁴ which reduced the computational requirements for such analysis. This method is based on a supercell approach with a single periodic structure. It mimics a random alloy concentration in a predefined crystal motif by selecting randomly the occupation of the atomic sites such that short-ranged, geometric correlations approximate

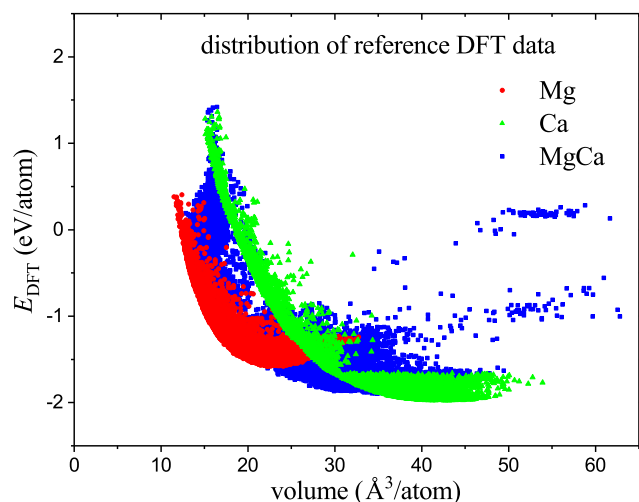


Fig. 1 Distribution of energies and volumes per atom in the DFT reference sets generated for Mg, Ca, and Mg-Ca with an evolutionary sampling as described in the text.

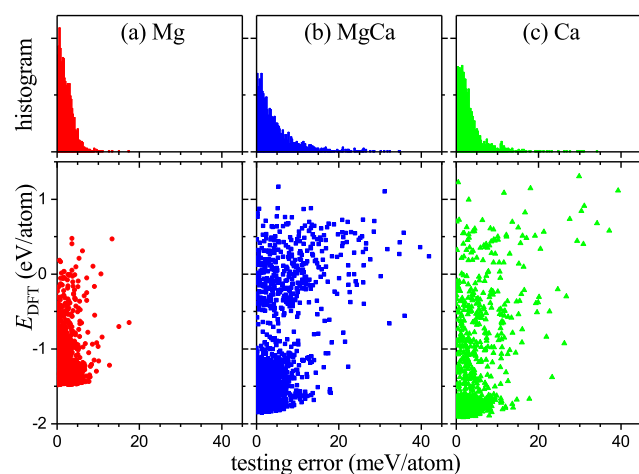


Fig. 2 Histograms of testing errors (top panels) and distributions of testing errors for sampled energy ranges (bottom panels) for the developed Mg-Ca neural network.

those of a perfectly random alloy. Our implementation follows the lines of the formalism introduced in ref.⁴⁴. In this paper, we have chosen only motifs that correspond to the basic crystals discussed below. We have optimized the supercell size to have a shape as cubic as possible, which leads to a more isotropic alloying distribution. As the number of considered phases is very large and the minimum number of atoms in the SQS supercell is around 160, we have only used the NN model to evaluate the formation energy. SQS method have been used for the binary Mg-Ca system but only for a few concentrations due to the high computational cost of the DFT.⁷⁷

2.5 Comparison between MHM-DFT and FF-NN

First, we performed benchmark structural searches using two different combinations, MHM-DFT and FF-NN, with the purpose of evaluating the methodologies' exploration capability and energy prediction quality. In this test, we restricted the structure sizes not to exceed 8 atoms per unit cell to ensure a fair comparison of the two approaches with manifestly different computational costs of evaluating a given candidate phase. Fig. 3 shows formation energies (top) and relative formation energies (bottom) for relevant low-energy phases generated in the two searches. The full statistical distribution of the number of potential metastable structures can be found in the SI.⁶³

Not unexpectedly, both approaches identified the 6-atom C15-Mg₇Ca₂ Laves phase, closely related to the known 12-atom C14-Mg₇Ca₂ ground state, to have the lowest formation energy across all compositions in the considered size-constrained space. No other compounds were found with either method to be closer than 6 meV/atom to the boundary of the convex hull defined by hcp-Mg, C15-Mg₇Ca₂, and fcc-Ca. The absence of any artificially stabilized phases in the FF-NN set attests to a sound PES mapping provided by the NN model. As an additional check of the NN accuracy on configurations not explicitly included in the training, we re-optimized and evaluated the near-stable FF-NN structures (bottom panel of Fig. 3) with the DFT. The average difference between the NN (purple diamonds) and DFT (blue circles) energies is about 2 meV/atom, significantly smaller than the ~ 7 meV/atom NN testing error. Our examination of the full MHM-DFT and FF-NN sets revealed that the former had a higher percentage of low-symmetry structures which could be only partly explained by the less stringent relaxation settings in the DFT calculations and that the latter had a larger number of distinct crystal structures. The results indicate that when it comes to finding metastable structures, the MHM and FF search engines explore the space differently and could be considered complementary.

3 Mg_(1-x)Ca_x (Meta)stable structures at 0, 5, and 10 GPa

Having observed a reliable performance of the FF-NN approach in our benchmark tests, we used the method for a large-scale exploration of the Mg-Ca configuration space. The search was performed at fixed Mg_{1-x}Ca_x compositions for structures with up to 28 atoms per unit cell at 5 GPa. The total number of structures found was close to 70,000, of which around 10,000 were deter-

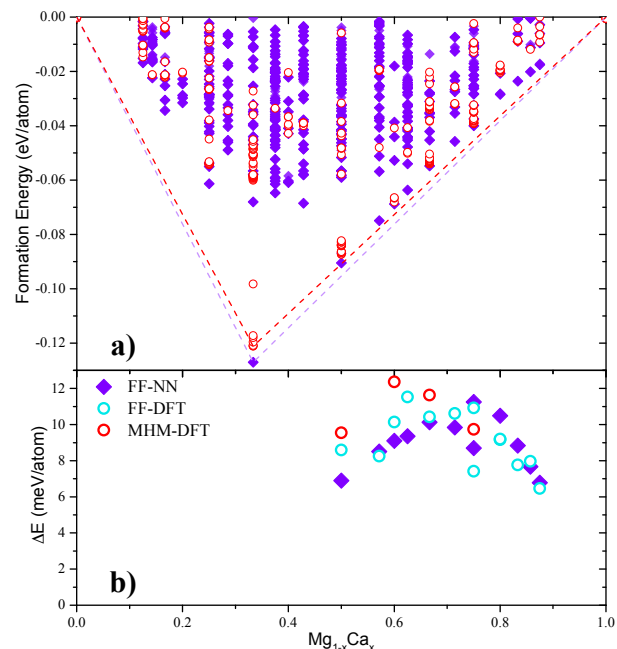


Fig. 3 (a) Formation energies for phases obtained with MHM-DFT (red circles) and with FF-NN (purple diamonds) at zero pressure and up to 8 atoms per cell. The convex hulls in both cases are defined by the C15-Mg₇Ca₂ Laves phase. (b) Energy difference with respect to the hcp-Mg ↔ C15-Mg₇Ca₂ ↔ fcc-Ca tie lines for low-energy phases in the MHM-DFT and FF-NN sets. The FF-NN structures were also re-optimized and evaluated with DFT (blue circles) to illustrate the NN model performance for (near)stable structures.

mined as non-duplicate based on the energy per atom and the pair correlation function. All the unique structures were subsequently relaxed at 0 and 10 GPa. The much lower computational cost required for local re-optimizations and the considerable size of the pool containing diverse (near)stable candidate structures allowed us to identify potentially synthesizable phases at different pressures.

Elemental ground states used as reference in the calculation of the formation energies were hcp-Mg (observed up to about ~ 50 GPa⁷⁸) and fcc-Ca (observed up to ~ 20 GPa⁷⁹). DFT approximations have been reported to predict lower values of the fcc to bcc transition pressure for Ca.⁸⁰ Since bcc was found in our calculations to be more stable than fcc by only 3.6 meV/atom at 10 GPa, the use of fcc-Ca as a reference in the 0-10 GPa range has an insignificant effect on the relative stability of the considered compounds.

Fig. 4 shows the resulting NN formation energies and the corresponding convex hull at 0 GPa. A small set of the most promising candidate phases was examined in more detail at both the NN and DFT levels. Fig. 5 illustrates the evolution of the DFT relative enthalpy for select phases relative to the tie lines defined by hcp-Mg, C14-Mg₂Ca, and fcc-Ca. Phase B2-MgCa becomes stable above 2 GPa of pressure. Two cF16-Mg₃Ca and hP8-MgCa₃ phases have high relative enthalpy at 0 GPa but quickly stabilize under compression. As discussed below, C14-Mg₂Ca, C15-Mg₂Ca, C36-Mg₂Ca, mS18-Mg₇Ca₂, and mS18-Mg₇Ca₂ have

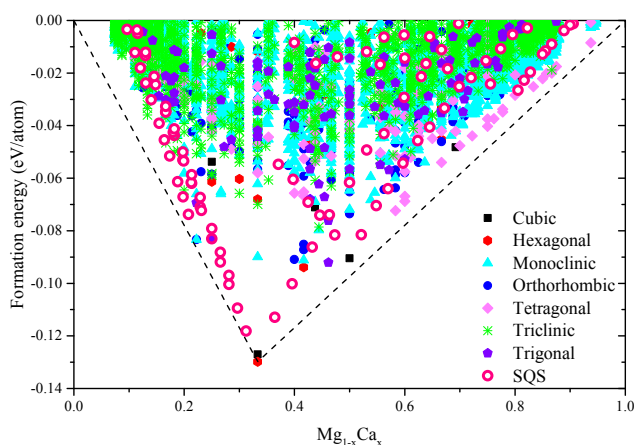


Fig. 4 Convex hull at 0 GPa of pressure for $\text{Mg}_{1-x}\text{Ca}_x$ binary compounds. We have categorized the structures by symmetry. Open pink circles represent low-energy configurations of SQS phases, where Mg_2Ca , Mg_7Ca_2 , Mg_2Ca_7 , and MgCa were used as motifs.

common structural morphologies which explains why pressure and temperature have a much less pronounced effect on their relative stability. According to the DFT formation enthalpy results (Figs. 4-6), the convex hulls at 0, 5, and 10 GPa are defined by one ($\text{C14-Mg}_2\text{Ca}$), two ($\text{C14-Mg}_2\text{Ca}$ and B2-MgCa), and three ($\text{C14-Mg}_2\text{Ca}$, B2-MgCa , and $\text{cF16-Mg}_3\text{Ca}$) phases, respectively. The transition pressures predicted with the NN and DFT methods are in a fairly good agreement and consistent with the ~ 7 meV/atom accuracy of the NN model. The respective NN and DFT values are 1.9 GPa and 1.7 GPa for B2-MgCa ; 10.0 GPa and 7.5 GPa for $\text{cF16-Mg}_3\text{Ca}$; and 5.5 GPa and 12 GPa for hP8-MgCa_3 . Our phonon calculations indicated that the aforementioned low-enthalpy phases are dynamically stable under ambient pressure with the exception of hP8-MgCa_3 which has no imaginary phonon frequencies only when compressed, e.g., at 10 GPa.

In order to evaluate the role of disorder on the stability of Mg-Ca compounds at ambient pressure we created a set of SQS with stoichiometries ranging from $x = 0.1$ up to $x = 0.9$. We used (meta)stable crystal phases corresponding to the Mg_2Ca , Mg_7Ca_2 , Mg_2Ca_7 , and MgCa compositions observed to be near the tie line at 0 GPa. All phases were considered by using randomness over the magnesium sublattice as well as for the two-sublattices (Ca and Mg). SQS phases could give an important insight of the role of site disorder or mixing in Mg-Ca binary system. The NN-based calculations showed that the Mg-rich disordered phases stay closer to the convex hull compared to the Ca-rich disordered counterparts. This agrees with the work of Zhong et al.⁷⁷ where the authors show that enthalpy of mixing at 298.15 K of either fully relaxed or symmetry preserved SQS structures with concentration of $x=0.666$ deviates from values of the ideal mixing (roughly 0.04 eV/atom). Contrary to what happens for concentration $x=0.166$, where both, symmetry preserved and fully relaxed, stay close to the results of ideal mixing. Supercells of around 216 atoms were considered for the SQS and they were evaluated by means of the NN method. The large number of atoms in the cell makes difficult to estimate the enthalpy

of mixing accurately since it is necessary to determine interaction parameters and the site fraction in each sublattice as discussed in ref.⁷⁷ (see Fig. S6). It is not a surprise that SQS phases exhibit higher formation energy with respect to local relaxations.⁸¹ However, this was only expected for the $x=1/3$ since this phase is the only known stable compound of the Mg-Ca binary system and we also found this result for $x=0.222$.

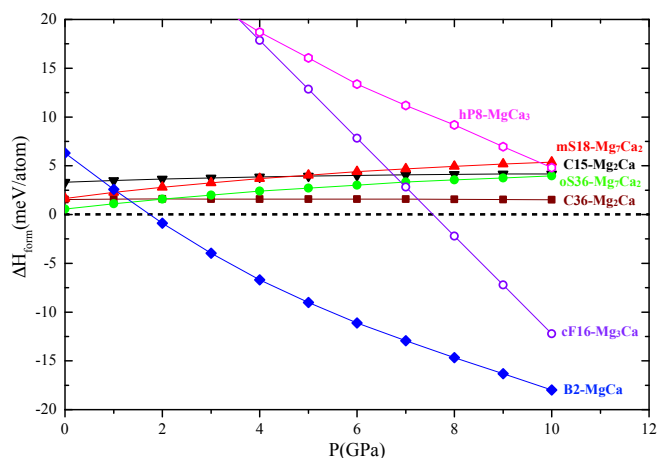


Fig. 5 Pressure dependence of the relative enthalpy (calculated at DFT level) for identified Mg-Ca candidate materials with respect to the $\text{hcp-Mg} \leftrightarrow \text{C14-Mg}_2\text{Ca} \leftrightarrow \text{fcc-Ca}$ convex hull.

4 Properties of (meta)stable Mg-Ca phases

In this section we discuss a set of phases determined to be at least metastable in the 0-10 GPa range in our structural searches: $\text{oS36-Mg}_7\text{Ca}_2$ and $\text{mS18-Mg}_7\text{Ca}_2$ at $x = 0.222$, $\text{cF16-Mg}_3\text{Ca}$ at $x = 0.25$, B2-MgCa at $x = 0.5$, $\text{hP8-Mg}_2\text{Ca}_6$ at $x = 0.75$, and $\text{C14-Mg}_2\text{Ca}$, $\text{C15-Mg}_2\text{Ca}$, and $\text{C36-Mg}_2\text{Ca}$ at $x = 0.333$. Table 2 summarizes key properties of potentially synthesizable Mg-Ca phases that, to the best of our knowledge, have not been studied before either theoretically or experimentally. The cif files for each of the structures are available in the SI.^{63,82} In what follows, electronic structure and density of states were calculated using DFT while phonon dispersions were obtained at the NN level. In addition, the Supplemental Information contains (i) atomic orbital projections of the electronic density of states (DOS) in Fig. S7; (ii) element-resolved phonon DOS in Fig. S8; and (iii) frequencies of phonon modes with either infrared or Raman response in Table S1.⁶³

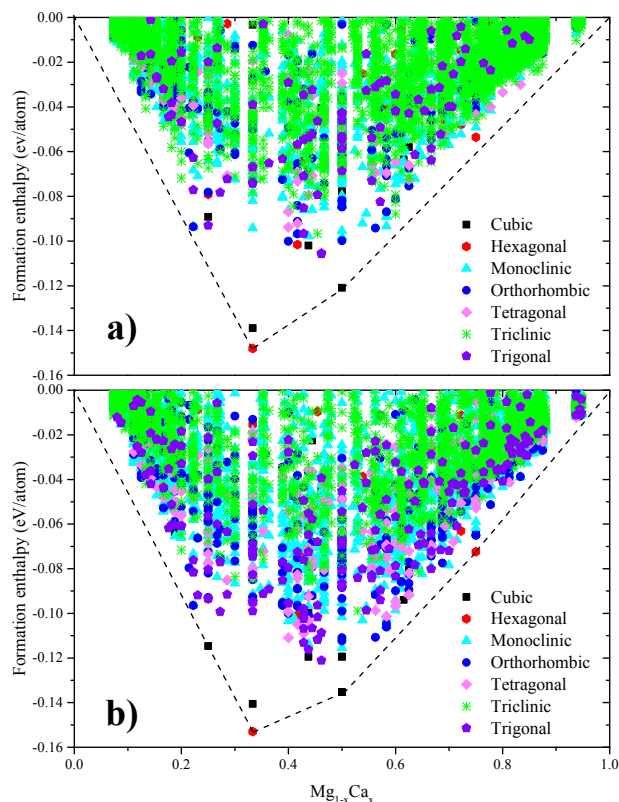


Fig. 6 Convex hull of $\text{Mg}_{1-x}\text{Ca}_x$ binary compounds at (a) 5 GPa and (b) 10 GPa of hydrostatic pressure.

Table 3 Calculated elastic constants, bulk (K), Shear (G) and Young (E) modulus and Poisson ratio (ν). Experimental and other theoretical values are also shown for the ground state structure. All the units are GPa. Data from ⁸³ corresponds to experimental measurements.

Phase	C11	C12	C13	C33	C44	K	G	E	ν
oS36- Mg_7Ca_2	63.6	19.4	10.4	71.6	21.3	31.5	22.9	55.2	0.207
mS18- Mg_7Ca_2	53.6	22.4	14.1	64.8	14.5	30.9	17.0	43.2	0.267
Mg_3Ca	39.6	25.3			27.9	30.3	19.6	48.3	0.233
MgCa	35.0	21.3			25.7	25.9	18.1	44.1	0.216
MgCa_3	55.3	46.0	16.7	91.3	48.9	40.2	12.9	35.0	0.355
C14	59.3	18.6	13.2	62.2	20.4	30.2	19.8	48.8	0.231
-C14 [⁸³]	61.2	17.6	15.0	65.5	19.2	31.4	21.3	52.3	
-C14 [⁸⁴]	53.7	22.9	10.1	66.8	14.6	28.9	17.7	44.1	0.246
C15	50.1	19.8			25.9	29.9	21.6	52.3	0.209

4.1 Mg_7Ca_2 ($x=0.222$)

The most promising candidate material uncovered in the FF-NN search was a monoclinic mS18- Mg_7Ca_2 phase with space group #12 ($C2/m$). The NN model placed it 3.2 meV/atom above the corresponding tie line at zero pressure while subsequent DFT calculations assessed the margin to be even smaller, only 1.7 meV/atom. The reason behind the near stability of the compound at such an unusual stoichiometry becomes evident upon examination of the mS18- Mg_7Ca_2 and C14- Mg_2Ca structural morphologies. The two structures can be represented as $\text{Mg}_3\text{-Ca-Mg}_2\text{-Mg}_2\text{-Ca}$ and $\text{Mg}_3\text{-Ca-Mg-Ca}$ stacking sequences, respectively (see Figs. 7-9). Therefore, mS18 can be obtained from C14 by changing the unit that bridges two neighboring Mg_3 kagome layers from a single Mg layer to two linked $\text{Mg}_2\text{-Mg}_2$ honeycomb layers (see Fig. 8). The close structural relationship helps explain why mS18- Mg_7Ca_2 ends up being so close to the tie line connecting hcp-Mg

Table 2 Lattice parameters, high and low group velocities, Debye and melting temperatures, and universal anisotropy index (UA) calculated with the NN interatomic potential for select Mg-Ca binary phases at 0 GPa. *The properties for hP8- MgCa_3 are given for the relaxed phase at 10 GPa. The DFT-optimized lattice parameters are given in brackets and the full structural information is provided in the SI.⁶³

	mS18- Mg_7Ca_2	oS36- Mg_7Ca_2	cF36- Mg_3Ca	B2-MgCa	hP8- MgCa_3 *
a (Å)	6.029 (6.081)	10.417 (10.334)	7.483 (7.480)	3.963 (3.967)	6.771 (6.723)
b (Å)	10.417 (10.359)	6.025 (6.079)			
c (Å)	7.922 (7.877)	15.281 (15.239)			5.430 (5.489)
β (deg)	105.207 (105.089)				
v_{high} (THz Å)	59.15	60.10	29.80	32.20	64.2
v_{low} (THz Å)	32.53	31.90	14.70	15.76	27.7
T_{Debye} (K)	340	398	336	312	175
T_{melting} (K)	893	899	887	847	793
UA	0.49	0.09	2.57	2.42	3.63

and C14- Mg_2Ca .

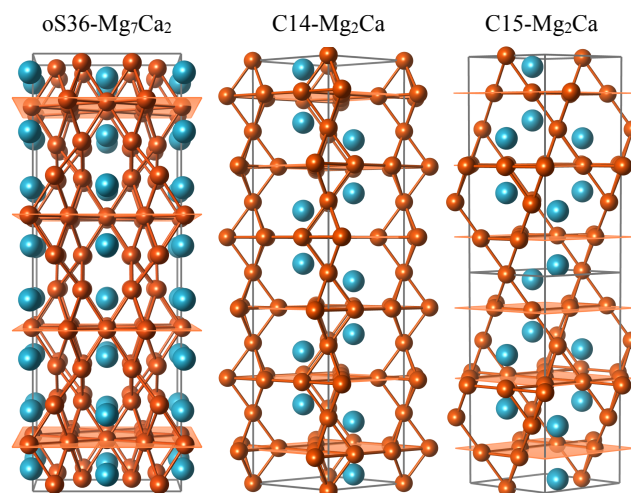


Fig. 7 Crystal structure of oS36- Mg_7Ca_2 (left), C14- Mg_2Ca (center), and C15- Mg_2Ca (right) in hexagonal representation. Mg kagome layers in each structure are illustrated with semitransparent planes. Orange and blue balls represent Mg and Ca atoms, respectively.

We proceeded to generate other stacking sequences at the 7:2 composition manually in an attempt to identify even more stable configurations. By doubling the c -axis and adjusting the layers' horizontal positions in mS18 we constructed a more symmetric oS36 variant with space group #63 ($Cmcm$). We found Mg_7Ca_2 to be indeed slightly more stable in the orthorhombic rather than the monoclinic form. The energy gain of 1.0 meV/atom calculated with DFT could be related to the change in the density of states (DOS) around the Fermi level. As demonstrated in Figs. 8-9, the high DOS at the Fermi level in mS18 is noticeably reduced in oS36 which is a common stabilization factor observed in other materials.^{85,86} The much smaller energy gain of 0.01 meV/atom produced by the NN model is not surprising because energy differences resulting from subtle variations in the electronic structure are not easily captured with classical models. In this case, the long-range stacking order modification leads to only minor changes in the local atomic environments starting with inter-

atomic distances around 3.6 Å. In principle, the FF-NN settings permitted the identification of structures with 18 atoms in the primitive unit cell and the resolution of candidate phases 0.01 meV/atom apart but oS36 proved to be a challenging metastable phase to find in unsupervised searches.

The mS18 and oS36 structures have been previously observed in Co_7Nb_2 ³⁴ and Ag_7Ca_2 ⁸⁷ compounds, respectively. Studies dedicated to Co_7Nb_2 provided a detailed analysis of the mS18 structure and linked an unexpected plastic deformability of the intermetallic compound to the particular layered morphology allowing easy dislocation glide on (001) planes.^{34,88} One of the consequences was the difficulty to obtain powder samples for XRD characterization. Similar challenges are likely to be encountered in the case of Mg_7Ca_2 .

We note that mS18 and oS36 were not available in the Inorganic Crystal Structure Database (ICSD)^{89,90} at the time of the *ab initio* high-throughput study of Mg alloys by Taylor et al.²¹ which explains why the near-stability of the Mg_7Ca_2 compound was not recognized before. The oS36- Ag_7Ca_2 phase is presently listed in the ICSD but neither mS18 nor oS36 has yet been considered for the Mg-Ca binary in the largest *ab initio* databases.^{91,92}

Since the application of pressure was determined not to stabilize the mS18 and oS36 phases (see Fig. 5), we investigated the effect of the vibrational entropy on their stability at high temperatures. Phonon dispersions calculated at the NN level showed no modes with imaginary frequencies and featured optical branches involving Mg vibrations with frequencies up to 8.8 THz (see Figs. 8-9). Once we added the entropy corrections to the free energies of hcp-Mg, mS18/oS36- Mg_7Ca_2 , and C14- Mg_2Ca , we discovered that the new phases do stabilize at elevated temperatures (see Fig. 10). Given the small energy scale, we also evaluated the relative free energy for mS18 at the DFT level for comparison (we were not able to obtain sufficiently converged phonon results for oS36 which could be caused by a multitude of issues at the DFT level^{57,86}). It is satisfying to see that the NN model agrees well with the DFT on predicting the $\Delta F(T)$ dependence. Accurate evaluation of the transition temperature is difficult with any method because the estimates are greatly affected by the systematic and numerical errors in the relative energy calculations. For example, our local density approximation⁹³ results indicated that mS18 and oS36 are already stable at $T = 0$ K by 1.1 and 2.2 meV/atom, respectively, which was the case for our predictions in other systems.⁹⁴ All our calculations suggest that oS36- Mg_7Ca_2 becomes thermodynamically stable at high temperatures and could be synthesizable. Tables 2-3 summarize crystal structures parameters, vibrational properties, elastic moduli, elastic constants, etc.

4.2 Mg_3Ca ($x=0.25$)

The cF16- Mg_3Ca phase with space group #225 ($Fm\bar{3}m$) exhibits a considerable stabilization under compression. As the formation enthalpy lowers from -0.053 eV/atom at 0 GPa down to -0.115 eV/atom at 10 GPa, the relative formation enthalpy goes from $+0.038$ meV/atom down to -0.012 meV/atom at the respective pressures in our DFT calculations in Fig. 5 (the NN calculations

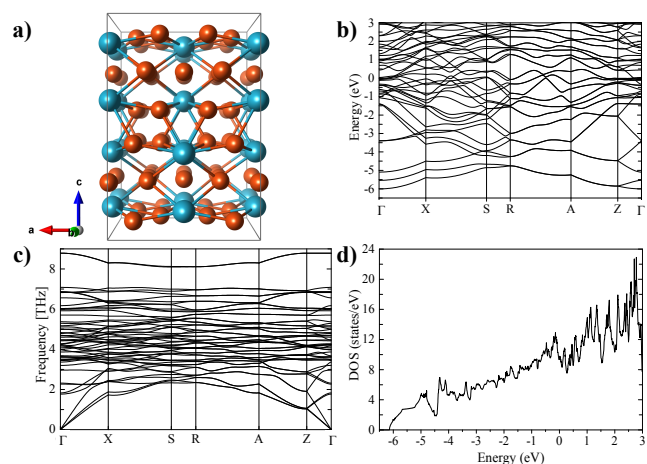


Fig. 8 (a) $1 \times 2 \times 1$ supercell of the crystal structure of oS36- Mg_7Ca_2 . (b) Electronic band structure along high symmetry paths in the irreducible Brillouin zone. (c) Phonon dispersion. (d) Electronic density of states.

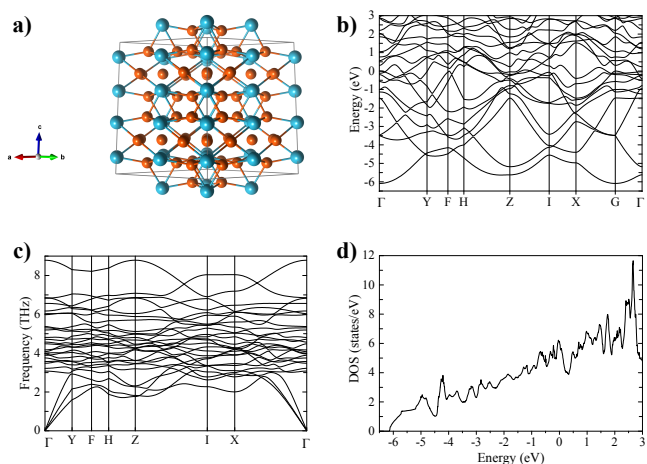


Fig. 9 (a) $2 \times 2 \times 2$ supercell of the crystal structure of mS18- Mg_7Ca_2 . (b) Electronic band structure along high symmetry paths in the irreducible Brillouin zone. (c) Phonon dispersion. (d) Electronic density of states.

show a similar -43 meV/atom drop). In contrast to the elemental ambient-pressure ground state structures, hcp for Mg and fcc for Ca, cF16 has the bcc underlying lattice. A distinctive feature of the lattice decoration in cF16- Mg_3Ca is that the larger Ca atoms are surrounded entirely by Mg neighbors in the first 8+6 shell. The stabilization of the binary bcc phase could be linked to the observed preference for both elements to adopt the bcc structure, although the transitions happen at higher pressures of ~ 50 GPa for Mg⁷⁸ and ~ 20 GPa for Ca.⁷⁹

These stability results can be rationalized by comparing atomic volumes in the competing phases. For the unit cells fully relaxed with the DFT, the difference in atomic volume for cF16 with respect to the mixture of bcc-Mg and bcc-Ca at 10 GPa is -0.59 Å³/atom. The cF16 relative compactness translates into a -37 meV/atom gain from the PV enthalpic term at that pressure. Compared to the mixture of hcp-Mg and C14- Mg_2Ca , cF16

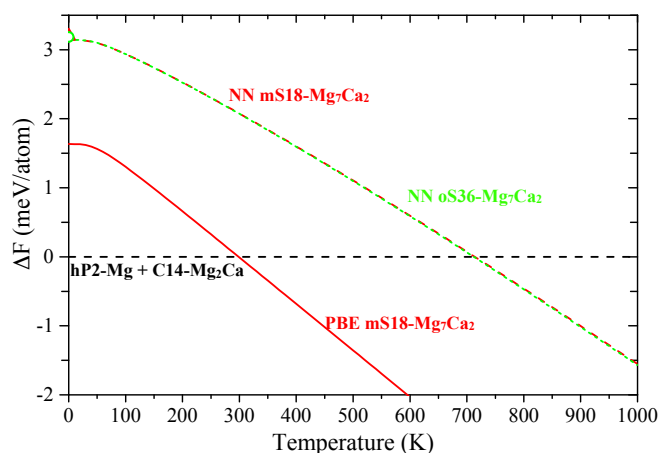


Fig. 10 Relative free energy as a function of temperature for mS18-Mg₇Ca₂ (red) and oS36-Mg₇Ca₂ (green) phases with respect to hcp-Mg and C14-Mg₂Ca. Dashed (solid) lines are NN (DFT) results.

has an even lower relative volume of $-0.80 \text{ \AA}^3/\text{atom}$ and a lower relative enthalpy of -50 meV/atom . Hence, the PV contribution is the dominant stabilization factor for cF16 which is a common case in high-pressure phase transformations.

Fig. 11 and Tables 2-3 summarize calculated properties for this phase at zero pressure. We note an unusually large universal anisotropy index (AU), close to that in such anisotropic materials as Sb and Pb.

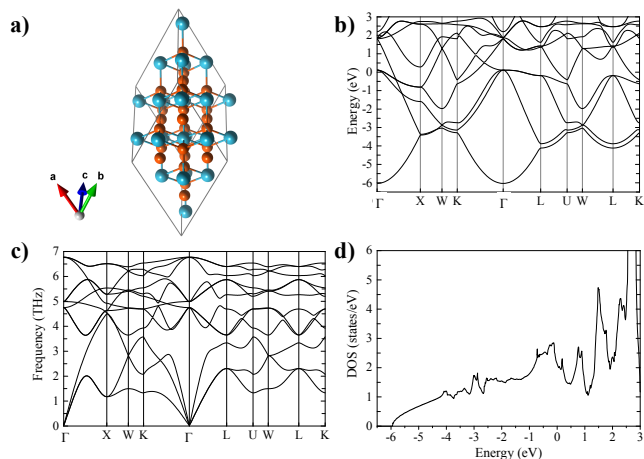


Fig. 11 (a) $2 \times 2 \times 2$ supercell of the crystal structure of cF16-Mg₃Ca. (b) Electronic band structure on selected high symmetry paths in the irreducible Brillouin zone. (c) Phonon dispersion. (d) Electronic density of states.

4.3 MgCa ($x=0.5$)

The lowest-enthalpy cP2-MgCa phase with space group #221 ($Pm-3m$) identified in the FF-NN search at the 1:1 composition is another example of an ordered binary bcc structure stabilized under compression. Mg and Ca occupy the corner (1a) and center

(1b) Wyckoff sites in this well-known B2 cesium chloride structure. B2-MgCa starts as a slightly metastable phase at 0 GPa just 6 meV/atom above the tie lines and defines the convex hull at both 5 and 10 GPa. The non-linear dependence of the relative enthalpy on pressure can be attributed to different compressibilities of the competing phases in this case. Namely, B2-MgCa has a noticeably lower value of the atomic volume, $-0.53 \text{ \AA}^3/\text{atom}$, relative to C14-Mg₂Ca and fcc-Ca at 0 GPa but only $-0.23 \text{ \AA}^3/\text{atom}$ at 10 GPa which explains the change in the $\Delta H(P)$ slope in Fig. 5. The resulting enthalpy gain of -14 meV/atom coming from the PV term is fairly modest and nearly matches the -18 meV/atom relative stability at 10 GPa. Compared to bcc-Mg and bcc-Ca, B2-MgCa essentially follows the Vegard's law at 10 GPa, as the relative atomic volume is $+0.03 \text{ \AA}^3/\text{atom}$.

The sound velocities (Table 2) and elastic constants (Table 3) are found to be very similar for the considered cubic B2-MgCa and cF14-Mg₃Ca phases. Both are close to those in the cubic binary Li-Mg phases.⁹

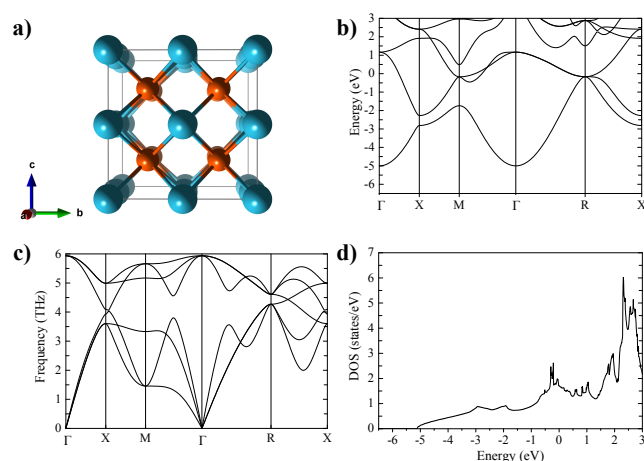


Fig. 12 (a) $2 \times 2 \times 2$ supercell of the crystal structure of B2-MgCa ($x=0.5$). (b) Electronic band structure on selected high symmetry paths in the irreducible Brillouin zone. (c) Phonon dispersion and (d) Electronic density of states.

4.4 MgCa₃ ($x=0.75$)

The FF-NN search suggested that hP8-MgCa₃ with space group # 194 ($P6_3/mmc$) becomes thermodynamically stable below 5.5 GPa and is -15 meV/atom below the C14-Mg₂Ca \leftrightarrow fcc-Ca tie line at 10 GPa. Subsequent DFT calculations indicated that the transition should happen at a higher pressure around 12 GPa, with the phase being metastable by $+5 \text{ meV/atom}$ at 10 GPa. The 20 meV/atom difference between the NN and DFT relative enthalpy values is noticeably higher than the $\sim 7 \text{ meV/atom}$ accuracy of the developed classical model but one should take into account that the evaluation of the relative stability in this case involved three phases leading to accumulation of errors. As mentioned above and demonstrated in Fig. 13 c), hP8-MgCa₃ is dynamically stable only at elevated pressures and is not expected to be quenchable down to ambient conditions. For this reason, we evaluated its

properties at 10 GPa where it is at least metastable (Tables 2-3). Structurally, hP8-MgCa₃ has the hcp lattice as the underlying motif which differs from the stable bcc-based morphology of cF16-Mg₃Ca and B2-MgCa.

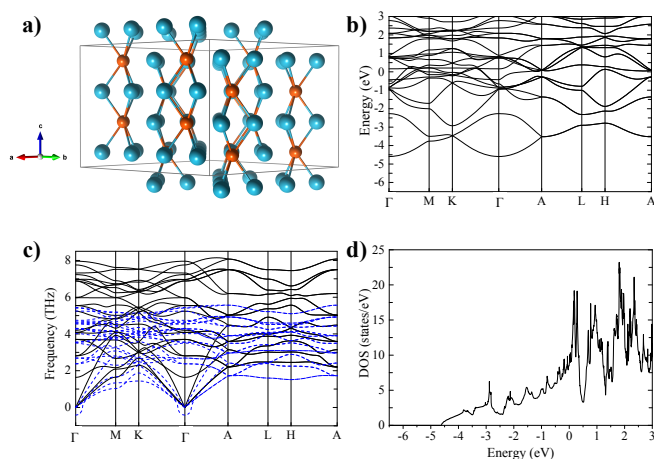


Fig. 13 (a) $2 \times 2 \times 2$ supercell of the crystal structure of hP8-MgCa₃ ($x=0.75$). (b) Electronic band structure on selected high-symmetry paths in the irreducible Brillouin zone. (c) Phonon dispersion at 0 (red-dashed) and at 10 GPa (black-solid). (d) Electronic density of states.

4.5 Mg₂Ca Laves phases

Extensive studies of Mg-based alloys have demonstrated that chemical composition is a critical factor determining the formation of a particular Laves type (see Fig. 7).^{12,21,95,96} For example, (pseudo)binary Laves phases in the Mg-Al-Ca ternary system have been observed to crystallize in all three C14, C15, and C36 types.^{12,95} At the Mg₂Ca composition, there have been no reports on the synthesis of any other Laves variants besides C14 despite several DFT studies showing C36 (C15) being metastable by only 4 (3) meV/atom⁹⁷, 0.5 (3.0) meV/atom¹⁷, 1 (4) meV/atom⁷⁷, 2.3 (4.3) meV/atom²¹, and 1.9 (3.0) meV/atom (present study) at $T = 0$ K. Surprisingly, the importance of the vibrational entropy on the relative stability of the Mg₂Ca Laves phases appears not to have been examined.

Fig. 15 shows relative free energies for C15 and C36 with the phonon entropic term calculated at both the DFT and the NN levels. As in the case of Mg₇Ca₂, the NN model reliably reproduced the temperature dependence of the free energy correction. The sub-meV/atom level of agreement between the NN and DFT results for the relative energies at zero temperature is likely fortuitous even under the assumption of significant error cancellations because of the Laves phases' similar morphologies. In fact, our test results in Fig. S5 illustrate that convergence of DFT relative energies to within 0.5 meV/atom requires dense k -point meshes which may explain the variance of the previously reported values. Given the large effect the numerical and systematic errors can have on the estimate of the transition temperature in this case, it is unclear whether the vibrational contribution could stabilize the C36 or C15 phase below the compound's melting temperature of

988 K. The apparent lack of success to observe the phases in numerous experiments suggests that they just miss becoming stable but it might be worth re-examining the high- T range around this composition.

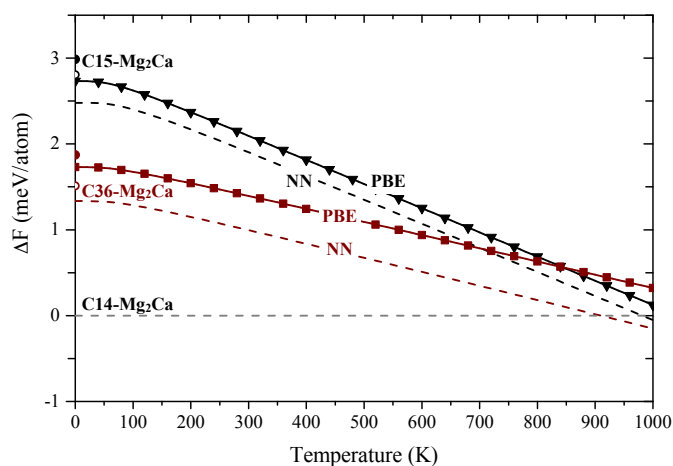


Fig. 14 Free energy difference with respect to the most stable structure C14 for 0 GPa.

We have calculated elastic constants for the three Laves phases. We have found that for the structure with hexagonal symmetry (C14) the elastic constants fulfill the following stability restrictions: $C_{11} > 0$, $C_{44} > 0$, $C_{11} - C_{12} > 0$ and $(C_{11} + C_{12})C_{33} - 2C_{13}^2 > 0$. This result agrees with previous theoretical calculations on the ground-state structure of Mg₂Ca⁸⁴. Accordingly, the C15 Laves phase satisfies the restrictions for cubic systems: $C_{11} > 0$, $C_{44} > 0$, $C_{11} - C_{12} > 0$ and $C_{11} + 2C_{12} > 0$. Table 3 summarizes the obtained elastic constants together with previous calculated and measured data.

4.6 Summary of Mg-Ca properties

The total and projected DOS results in Figs. 8, 9, 11-13, and S7 show that the considered Mg-Ca alloys have electronic features typical for good s-p(d) metals.^{20,97} Near the bottom of the valence s-p manifold, e.g., around -6.5 eV in Fig. 8(d), the Mg-Ca phases have DOS shapes corresponding to the nearly free electron 3D states. Around the Fermi level, the increased contribution from the Ca-d states is responsible for the appearance of more pronounced peaks in the DOS. The electronic states at the Fermi level have predominately Ca-d and Mg-p character. Fig. 15(a) shows the lowest energies of the s-p states as a function of alloy composition. The observed nearly linear dependence suggests a rather low sensitivity of the s-p band dispersion to the particular structure at the considered Mg-Ca stoichiometries.

In contrast, Figs. 15(b) and S8 reveal a significant dependence of the phonon mode frequencies on the structural morphology. The highest frequencies plotted as a function of the Mg-Ca composition split into two sets that can be distinguished by the underlying lattice type. The set displaying an almost linear dependence on the composition is based on close-packed structures while the three outliers feature kagome frameworks. The short-

est Mg-Mg distances that determine the highest-frequency optical modes are noticeably different: e.g., 3.18 Å in hcp-Mg, 3.01 Å in oS36/mS18-Mg₇Ca₂, 3.24 Å in cF16-Mg₃Ca, and 3.07 Å in C14-Mg₂Ca. According to the projected phonon DOS in Fig. S8, the high-frequency optical modes do not involve any Ca atoms in the oS36/mS18-Mg₇Ca₂ phases.

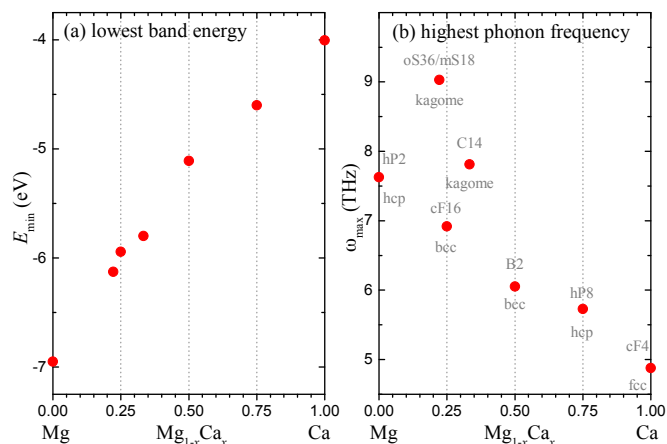


Fig. 15 (a) DFT energies of lowest valence states as a function of the Mg-Ca alloy composition. (b) Highest phonon frequencies calculated with the NN model for the considered Mg-Ca phases; the three outliers are phases with kagome lattices.

5 Conclusions

In this work we have demonstrated the viability of using NN interatomic potentials for a large-scale exploration of crystal structures at different compositions. The NN model trained in the stratified fashion on DFT data generated with evolutionary sampling has provided a sufficiently accurate and robust mapping of the PES to be used for unconstrained searches. In agreement with the DFT, it resolved low-energy phases with generally better than 7 meV/atom accuracy and correctly evaluated changes in the relative stability at high (P, T) conditions. Analysis of our FF-NN search results for Mg-Ca unit cells with up to 28 atoms has revealed several potentially synthesizable phases. At the 7:2 composition, mS18 and oS36 are promising candidates to be high- T ground states quenchable down to ambient conditions. At the 2:1 composition, the C36 and C15 Laves phases become comparable to the known C14 ground state in free energy at high T but the accuracy of the DFT/NN approximations is insufficient to determine definitively whether they would be thermodynamically stable below the melting point. At the 3:1 and 1:1 compositions, cF16 and B2 bcc-type structures are stabilized by pressure due to smaller relative volumes and are expected to form below 10 GPa. The identification of the (near)stable mS18/oS18-Mg₇Ca₂ phases is a good illustration of the need to complement high-throughput screening based on known prototypes with unconstrained searches. The latter may help avoid overlooking structure types that have yet to be observed or entered in major data depositories. Given the successful experimental confirmation of several predictions made with the MAISE's *evolutionary algorithm at the DFT level* in the Fe-B^{74,98}, Cr-B^{99,100}, Mn-B¹⁰¹⁻¹⁰³, Li-

B^{104,105}, Ca-B⁷⁵, and Na-Sn^{94,106} binaries, experimental observation of the new Mg-Ca materials would validate the presented hybrid search methodology based on *the FF search algorithm and the NN formalism* and open up new avenues in the development of light-weight alloys.

Conflicts of interest

There are no conflicts to declare.

Acknowledgments

This work used the Extreme Science and Engineering Discovery Environment (XSEDE), which is supported by National Science Foundation grant number OCI-1053575. Additionally, the authors acknowledge the support from Texas Advances Computer Center (TACC), Bridges supercomputer at Pittsburgh Supercomputer Center and Super Computing Systems (Spruce and Mountaineer) at West Virginia University (WVU). A.H.R. and W.I.H. acknowledge the support from National Science Foundation (NSF) DMREF-NSF 1434897, NSF OAC-1740111 and DOE DE-SC0016176 projects. A.N.K. and S.H. acknowledge the NSF support (Award No. DMR-1410514). W.I.H and A.B.H acknowledge the support from the grant "CONACyT Repatriación 2017" and the computational time provided by the Laboratorio Nacional de Supercomputo del Sureste de México.

References

- 1 S. Schumann and H. E. Friedrich, *Magnesium Alloys* 2003, 2003, pp. 51–56.
- 2 H. Zhang, S. Shang, J. E. Saal, A. Saengdeejing, Y. Wang, L.-Q. Chen and Z.-K. Liu, *Intermetallics*, 2009, **17**, 878 – 885.
- 3 E. F. Emley, *Principles of magnesium technology*, Oxford, New York, Pergamon Press, 1966.
- 4 A. Suzuki, N. Saddock, J. Jones and T. Pollock, *Acta Materialia*, 2005, **53**, 2823 – 2834.
- 5 J. Nie, *Scripta Materialia*, 2003, **48**, 981 – 984.
- 6 B. Mordike and T. Ebert, *Materials Science and Engineering: A*, 2001, **302**, 37 – 45.
- 7 A. Luo and M. O. Pekguleryuz, *Journal of Materials Science*, 1994, **29**, 5259–5271.
- 8 D. Zhou, J. Liu, P. Peng, L. Chen and Y. Hu, *Materials Letters*, 2008, **62**, 206 – 210.
- 9 O. Pavlic, W. Ibarra-Hernández, I. Valencia-Jaime, S. Singh, G. A. no Franco, D. Raabe and A. H. Romero, *Journal of Alloys and Compounds*, 2017, **691**, 15 – 25.
- 10 H. Somekawa, A. Singh and T. Mukai, *Scripta Materialia*, 2007, **56**, 1091 – 1094.
- 11 Y. Zhu, A. Morton and J. Nie, *Scripta Materialia*, 2008, **58**, 525 – 528.
- 12 R. Ninomiya, T. Ojio and K. Kubota, *Acta Metallurgica et Materialia*, 1995, **43**, 669 – 674.
- 13 L. Shao, T.-T. Shi, J. Zheng, X.-Z. Pan and B.-Y. Tang, *Intermetallics*, 2015, **65**, 29 – 34.
- 14 J. Jayaraj, C. Mendis, T. Ohkubo, K. Oh-ishi and K. Hono, *Scripta Materialia*, 2010, **63**, 831 – 834.
- 15 Y. Liu, W.-C. Hu, D.-J. Li, K. Li, H.-L. Jin, Y.-X. Xu, C.-S. Xu

- and X.-Q. Zeng, *Computational Materials Science*, 2015, **97**, 75 – 85.
- 16 W. PEARSON, *A Handbook of LATTICE SPACINGS AND STRUCTURES OF METALS AND ALLOYS*, Pergamon, 1967.
- 17 H. Zhang, S.-L. Shang, Y. Wang, L.-Q. Chen and Z.-K. Liu, *Intermetallics*, 2012, **22**, 17 – 23.
- 18 P. Mao, B. Yu, Z. Liu, F. Wang and Y. Ju, *Computational Materials Science*, 2014, **88**, 61 – 70.
- 19 S. Groh, *Journal of the Mechanical Behavior of Biomedical Materials*, 2015, **42**, 88 – 99.
- 20 P. Zhou and H. Gong, *Journal of the Mechanical Behavior of Biomedical Materials*, 2012, **8**, 154 – 164.
- 21 R. H. Taylor, S. Curtarolo and G. L. W. Hart, *Phys. Rev. B*, 2011, **84**, 084101.
- 22 K.-H. Kim, J. B. Jeon and B.-J. Lee, *Calphad*, 2015, **48**, 27 – 34.
- 23 S. Amerioun, S. I. Simak and U. Häussermann, *Inorganic Chemistry*, 2003, **42**, 1467–1474.
- 24 T. Rezukhina and L. Kravchenko, *The Journal of Chemical Thermodynamics*, 1972, **4**, 655 – 667.
- 25 P. Rennert and A. M. Radwan, *physica status solidi (b)*, 1976, **77**, 615–621.
- 26 J. Hafner, *Phys. Rev. B*, 1980, **21**, 406–426.
- 27 F. Stein, M. Palm and G. Sauthoff, *Intermetallics*, 2005, **13**, 1056 – 1074.
- 28 O. Carlson and D. Alexander, *Journal of the Less Common Metals*, 1968, **15**, 361 – 370.
- 29 K. Kumar and D. Miracle, *Intermetallics*, 1994, **2**, 257 – 274.
- 30 D. Arias and J. P. Abriata, *Bulletin of Alloy Phase Diagrams*, 1986, **7**, 237–244.
- 31 S. Kanazawa, Y. Kaneno, H. Inoue, W.-Y. Kim and T. Takasugi, *Intermetallics*, 2002, **10**, 783 – 792.
- 32 A. Taylor, N. Doyle and B. Kagle, *Journal of the Less Common Metals*, 1961, **3**, 265 – 280.
- 33 G. Shao, *Intermetallics*, 2002, **10**, 429 – 434.
- 34 F. Stein, D. Jiang, M. Palm, G. Sauthoff, D. GrÅijner and G. Kreiner, *Intermetallics*, 2008, **16**, 785 – 792.
- 35 D. T. Peterson, P. F. Diljak and C. L. Vold, *Acta Crystallographica*, 1956, **9**, 1036–1037.
- 36 O. Kubaschewski, *iron?Binary Phase Diagrams*, Springer, Berlin, Germany, 1982.
- 37 B. Kotur, E. Gratz, E. Bauer, G. Hilscher, A. Kottar, H. Michor, C. Reichl, G. Wiesinger and A. Markosyan, *Journal of Alloys and Compounds*, 1998, **278**, 49 – 59.
- 38 J. F. Cannon, D. L. Robertson, H. Hall and A. Lawson, *Journal of the Less Common Metals*, 1973, **31**, 174 – 176.
- 39 N. L. Eatough and H. T. Hall, *Inorganic Chemistry*, 1972, **11**, 2608–2609.
- 40 P. C. Sahu and N. V. Chandra Shekar, *Pramana*, 2000, **54**, 685–708.
- 41 Y. Liu, J. D. Livingston and S. M. Allen, *Metallurgical Transactions A*, 1992, **23**, 3303–3308.
- 42 Y. Liu, S. M. Allen and J. D. Livingston, *MRS Proceedings*, 1992, **288**, 203.
- 43 R. L. Johannes, R. Haydock and V. Heine, *Phys. Rev. Lett.*, 1976, **36**, 372–376.
- 44 A. Zunger, S.-H. Wei, L. Ferreira and J. E. Bernard, *Physical Review Letters*, 1990, **65**, 353.
- 45 P. Hohenberg and W. Kohn, *Phys. Rev.*, 1964, **136**, B864–B871.
- 46 W. Kohn and L. J. Sham, *Phys. Rev.*, 1965, **140**, A1133–A1138.
- 47 G. Kresse and J. Hafner, *Phys. Rev. B*, 1993, **47**, 558–561.
- 48 G. Kresse and J. Hafner, *Phys. Rev. B*, 1994, **49**, 14251–14269.
- 49 G. Kresse and J. Furthmüller, *Phys. Rev. B*, 1996, **54**, 11169–11186.
- 50 H. J. Monkhorst and J. D. Pack, *Phys. Rev. B*, 1976, **13**, 5188–5192.
- 51 G. Kresse and D. Joubert, *Phys. Rev. B*, 1999, **59**, 1758–1775.
- 52 P. E. Blöchl, *Phys. Rev. B*, 1994, **50**, 17953–17979.
- 53 H. B. Schlegel, *Journal of Computational Chemistry*, 1982, **3**, 214–218.
- 54 <http://maise-guide.org>.
- 55 A. Togo and I. Tanaka, *Scr. Mater.*, 2015, **108**, 1–5.
- 56 D. Alfé, *Computer Physics Communications*, 2009, **180**, 2622 – 2633.
- 57 S. Hajinazar, J. Shao and A. N. Kolmogorov, *Phys. Rev. B*, 2017, **95**, 014114.
- 58 M. Amsler and S. Goedecker, *The Journal of Chemical Physics*, 2010, **133**, 224104.
- 59 S. Singh, W. Ibarra-Hernández, I. Valencia-Jaime, G. Avendaño Franco and A. H. Romero, *Phys. Chem. Chem. Phys.*, 2016, **18**, 29771–29785.
- 60 S. Singh, A. C. Garcia-Castro, I. Valencia-Jaime, F. Muñoz and A. H. Romero, *Phys. Rev. B*, 2016, **94**, 161116.
- 61 G. Avendaño Franco and A. H. Romero, *Journal of Chemical Theory and Computation*, 2016, **12**, 3416–3428.
- 62 *PyChemia*, <https://github.com/MaterialsDiscovery/PyChemia>, Accessed: 2015-07-12.
- 63 Supplemental Material.
- 64 J. Behler and M. Parrinello, *Phys. Rev. Lett.*, 2007, **98**, 146401.
- 65 T. B. Blank, S. D. Brown, A. W. Calhoun and D. J. Doren, *The Journal of Chemical Physics*, 1995, **103**, 4129–4137.
- 66 A. P. Bartók, R. Kondor and G. Csányi, *Phys. Rev. B*, 2013, **87**, 184115.
- 67 S. A. Ghasemi, A. Hofstetter, S. Saha and S. Goedecker, *Phys. Rev. B*, 2015, **92**, 045131.
- 68 N. Artrith, A. Urban and G. Ceder, *Phys. Rev. B*, 2017, **96**, 014112.
- 69 R. Kobayashi, D. Giofré, T. Junge, M. Ceriotti and W. A. Curtin, *Phys. Rev. Materials*, 2017, **1**, 053604.
- 70 A. Khorshidi and A. A. Peterson, *Computer Physics Communications*, 2016, **207**, 310 – 324.
- 71 S.-D. Huang, C. Shang, X.-J. Zhang and Z.-P. Liu, *Chem. Sci.*,

- 2017, **8**, 6327–6337.
- 72 B. Jörg, *Angewandte Chemie International Edition*, 2017, **56**, 12828–12840.
- 73 J. Kang, S. H. Noh, J. Hwang, H. Chun, H. Kim and B. Han, *Phys. Chem. Chem. Phys.*, 2018, –.
- 74 A. N. Kolmogorov, S. Shah, E. R. Margine, A. F. Bialon, T. Hammerschmidt and R. Drautz, *Phys. Rev. Lett.*, 2010, **105**, 217003.
- 75 A. N. Kolmogorov, S. Shah, E. R. Margine, A. K. Kleppe and A. P. Jephcoat, *Phys. Rev. Lett.*, 2012, **109**, 075501.
- 76 V. L. Deringer, C. J. Pickard and G. Csányi, *Phys. Rev. Lett.*, 2018, **120**, 156001.
- 77 Y. Zhong, K. Ozturk, J. O. Sofo and Z.-K. Liu, *Journal of Alloys and Compounds*, 2006, **420**, 98 – 106.
- 78 G. W. Stinton, S. G. MacLeod, H. Cynn, D. Errandonea, W. J. Evans, J. E. Proctor, Y. Meng and M. I. McMahon, *Phys. Rev. B*, 2014, **90**, 134105.
- 79 H. Olijnyk and W. Holzappel, *Physics Letters A*, 1984, **100**, 191 – 194.
- 80 A. R. Oganov, Y. Ma, Y. Xu, I. Errea, A. Bergara and A. O. Lyakhov, *Proceedings of the National Academy of Sciences*, 2010, **107**, 7646–7651.
- 81 D. Shin, R. Arróyave, Z.-K. Liu and A. Van de Walle, *Phys. Rev. B*, 2006, **74**, 024204.
- 82 K. Momma and F. Izumi, *Journal of Applied Crystallography*, 2011, **44**, 1272–1276.
- 83 A. Sumer and J. F. Smith, *Journal of Applied Physics*, 1962, **33**, 2283–2286.
- 84 Z. Yang, J. Du, B. Wen, C. Hu and R. Melnik, *Intermetallics*, 2013, **32**, 156 – 161.
- 85 A. N. Kolmogorov and S. Curtarolo, *Phys. Rev. B*, 2006, **74**, 224507.
- 86 E. D. Sandoval, S. Hajinazar and A. N. Kolmogorov, *Phys. Rev. B*, 2016, **94**, 094105.
- 87 D. C. Fredrickson, *Journal of the American Chemical Society*, 2011, **133**, 10070–10073.
- 88 A. Leineweber, G. Kreiner, D. Gräijner, R. Dinnebier and F. Stein, *Intermetallics*, 2012, **25**, 34 – 41.
- 89 G. Bergerhoff, R. Hundt, R. Sievers and I. D. Brown, *Journal of Chemical Information and Computer Sciences*, 1983, **23**, 66–69.
- 90 A. Belsky, M. Hellenbrandt, V. L. Karen and P. Luksch, *Acta Crystallographica Section B*, 2002, **58**, 364–369.
- 91 S. Curtarolo, W. Setyawan, G. L. Hart, M. Jahnatek, R. V. Chepulskii, R. H. Taylor, S. Wang, J. Xue, K. Yang, O. Levy, M. J. Mehl, H. T. Stokes, D. O. Demchenko and D. Morgan, *Computational Materials Science*, 2012, **58**, 218 – 226.
- 92 A. Jain, S. P. Ong, G. Hautier, W. Chen, W. D. Richards, S. Dacek, S. Cholia, D. Gunter, D. Skinner, G. Ceder and K. A. Persson, *APL Materials*, 2013, **1**, 011002.
- 93 J. P. Perdew and A. Zunger, *Phys. Rev. B*, 1981, **23**, 5048–5079.
- 94 J. Shao, C. Beaufils and A. N. Kolmogorov, *Scientific Reports*, 2016, **6**, 28369.
- 95 A. Suzuki, N. Saddock, J. Jones and T. Pollock, *Scripta Materialia*, 2004, **51**, 1005 – 1010.
- 96 K. Ozturk, Y. Zhong, Z.-K. Liu and A. A. Luo, *JOM*, 2003, **55**, 40–44.
- 97 W.-Y. Yu, N. Wang, X.-B. Xiao, B.-Y. Tang, L.-M. Peng and W.-J. Ding, *Solid State Sciences*, 2009, **11**, 1400 – 1407.
- 98 H. Gou, N. Dubrovinskaia, E. Bykova, A. A. Tsirlin, D. Kasinathan, W. Schnelle, A. Richter, M. Merlini, M. Hanfland, A. M. Abakumov, D. Batuk, G. Van Tendeloo, Y. Nakajima, A. N. Kolmogorov and L. Dubrovinsky, *Phys. Rev. Lett.*, 2013, **111**, 157002.
- 99 A. F. Bialon, T. Hammerschmidt, R. Drautz, S. Shah, E. R. Margine and A. N. Kolmogorov, *Applied Physics Letters*, 2011, **98**, 081901.
- 100 H. Niu, J. Wang, X.-Q. Chen, D. Li, Y. Li, P. Lazar, R. Podloucky and A. N. Kolmogorov, *Phys. Rev. B*, 2012, **85**, 144116.
- 101 A. V. D. Geest and A. Kolmogorov, *Calphad*, 2014, **46**, 184 – 204.
- 102 K. Arno, L. Christian, G. N. C., B. Jakoah, W. Norbert, B. Johannes, K. J. A., S. Ram and A. Barbara, *Angewandte Chemie International Edition*, 2014, **53**, 1684–1688.
- 103 H. Niu, X.-Q. Chen, W. Ren, Q. Zhu, A. R. Oganov, D. Li and Y. Li, *Phys. Chem. Chem. Phys.*, 2014, **16**, 15866–15873.
- 104 A. N. Kolmogorov and S. Curtarolo, *Phys. Rev. B*, 2006, **73**, 180501.
- 105 A. N. Kolmogorov, S. Hajinazar, C. Angyal, V. L. Kuznetsov and A. P. Jephcoat, *Phys. Rev. B*, 2015, **92**, 144110.
- 106 J. M. Stratford, M. Mayo, P. K. Allan, O. Pecher, O. J. Borkiewicz, K. M. Wiaderek, K. W. Chapman, C. J. Pickard, A. J. Morris and C. P. Grey, *Journal of the American Chemical Society*, 2017, **139**, 7273–7286.